

Deconfined quantum criticality with emergent symmetry in the extended Shastry-Sutherland model

Wen-Yuan Liu,¹ Xiao-Tian Zhang,² Zhe Wang,³ Shou-Shu Gong,⁴ Wei-Qiang Chen,^{5,6} and Zheng-Cheng Gu⁷

¹*Division of Chemistry and Chemical Engineering, California Institute of Technology, Pasadena, California 91125, USA*

²*School of Physics, Beihang University, Beijing 100191, China*

³*Department of Physics, Beijing Normal University, Beijing 100875, China*

⁴*School of Physical Sciences, Great Bay University, Dongguan 523000, China, and
Great Bay Institute for Advanced Study, Dongguan 523000, China*

⁵*Institute for Quantum Science and Engineering and Department of Physics,
Southern University of Science and Technology, Shenzhen 518055, China*

⁶*Shenzhen Key Laboratory of Advanced Quantum Functional Materials and Devices,
Southern University of Science and Technology, Shenzhen 518055, China*

⁷*Department of Physics, The Chinese University of Hong Kong, Shatin, New Territories, Hong Kong, China
(Dated: September 21, 2023)*

Motivated by the exotic critical phenomena observed in the Shastry-Sutherland material $\text{SrCu}_2(\text{BO}_3)_2$ [Jimenez *et al*, *Nature* **592**, 370 (2021); Cui *et al*, *Science* **380**, 1179 (2023)], we investigate the ground state nature of the extended Shastry-Sutherland model (SSM) by the state-of-the-art 2D tensor network method. Via large-scale simulations up to 20×20 sites, we identify a continuous phase transition between the plaquette valence-bond solid (PVBS) phase and the antiferromagnetic (AFM) phase accompanied by an emergent $\text{O}(4)$ symmetry, which strongly suggests a deconfined quantum critical point (DQCP). Furthermore, we map out the phase diagram of the extended SSM and observe the same type of DQCP phenomena with emergent $\text{O}(4)$ symmetry and similar critical exponents along the whole critical line. Our results indicate a compelling scenario for understanding the origin of the proximate DQCP observed in recent experiments.

Introduction. In recent years, frustrated magnets have become a fascinating subject for exploring exotic quantum phenomena. One prominent example is the deconfined quantum critical point (DQCP), which suggests a new framework for understanding unconventional continuous transitions beyond the standard Landau-Ginzburg-Wilson (LGW) paradigm [1, 2]. While extensive numerical simulations have unraveled surprising phenomena related to the DQCP in various models [3–25] such as the emergent symmetry [7, 17], experimental example remains rare. Recently, experimental studies of the potential DQCP phenomena have made remarkable strides based on the layered frustrated magnetic compound $\text{SrCu}_2(\text{BO}_3)_2$ [26–28]. In particular, the observed magnetic field-driven PVBS-AFM transition in $\text{SrCu}_2(\text{BO}_3)_2$ displays extraordinary characteristics, including quantum critical scaling and emergence of $\text{O}(3)$ symmetry, suggesting a nearby DQCP [28].

The quasi-2D spin-1/2 compound $\text{SrCu}_2(\text{BO}_3)_2$ can be effectively described by the Shastry-Sutherland model [29, 30] (SSM), with the following Hamiltonian:

$$H = J_1 \sum_{\langle i,j \rangle} \mathbf{S}_i \cdot \mathbf{S}_j + J_2 \sum_{\langle\langle i,j \rangle\rangle} \mathbf{S}_i \cdot \mathbf{S}_j, \quad (1)$$

where J_1 and J_2 terms sum over all the nearest-neighbor (NN) [gray lines in Fig. 1(b)] and part of the next-nearest-neighbor (NNN) AFM Heisenberg interactions [red dashed lines denoted as J_{2a} in Fig. 1(b)] on the square lattice. It is a dimer valence-bond solid (DVBS) phase for small J_1/J_2 and an AFM phase for large J_1/J_2 . The existence of a plaquette VBS phase (PVBS) between the DVBS and AFM phases has also been well established, and the DVBS-PVBS transition is first order [26–28, 31–41]. Nevertheless, the physical nature of PVBS-AFM transition remains unresolved, being a critical concern for understanding the proximate DQCP phenomena

of $\text{SrCu}_2(\text{BO}_3)_2$ both theoretically and experimentally [26–28, 31, 33, 35–39, 41, 42].

Specifically, whether the potential PVBS-AFM transition belongs to first-order, a DQCP, or is extended to a gapless quantum spin liquid (QSL) phase in between is a big enigma. Series expansion study shows a continuous PVBS-AFM transition at $J_1/J_2 = 0.86(1)$ [42, 43], but infinite-size tensor network studies suggest a weakly first-order transition around $J_1/J_2 \approx 0.78$ [31, 35] and a multicritical point as a DQCP by introducing additional interactions [35]. In recent density matrix renormalization group (DMRG) studies, significantly different conclusions have also been found. While an earlier infinite-size DMRG (iDMRG) study suggests a direct PVBS-AFM transition, which is further argued to represent a DQCP with emergent $\text{O}(4)$ symmetry based on quantum field theory analyses [33], a recent DMRG level crossing study indicates an intermediate gapless QSL phase between the PVBS and AFM phases for $0.79 \lesssim J_1/J_2 \lesssim 0.82$ [37]. The latter proposition is also supported by a functional renormalization group study [36]. These controversial results lead to different scenarios for understanding the proximate DQCP phenomena in $\text{SrCu}_2(\text{BO}_3)_2$ under magnetic fields in recent experiment [28].

In this paper, we employ the state-of-the-art tensor network simulations by means of the finite projected entangled pair state (PEPS) approach to study the extended SSM with the following Hamiltonian:

$$H = J_1 \sum_{\langle i,j \rangle} \mathbf{S}_i \cdot \mathbf{S}_j + J_{2a} \sum_{\langle\langle i,j \rangle\rangle} \mathbf{S}_i \cdot \mathbf{S}_j + J_{2b} \sum_{\langle\langle i,j \rangle\rangle} \mathbf{S}_i \cdot \mathbf{S}_j, \quad (2)$$

where J_{2a} and J_{2b} represent two sets of the next-nearest-neighbor (NNN) interactions on the square lattice. In the limit $J_{2b} = 0$ (or $J_{2a} = 0$), the model recovers the well known SSM, while with $J_{2a} = J_{2b}$ it is the checkerboard model (CBM).

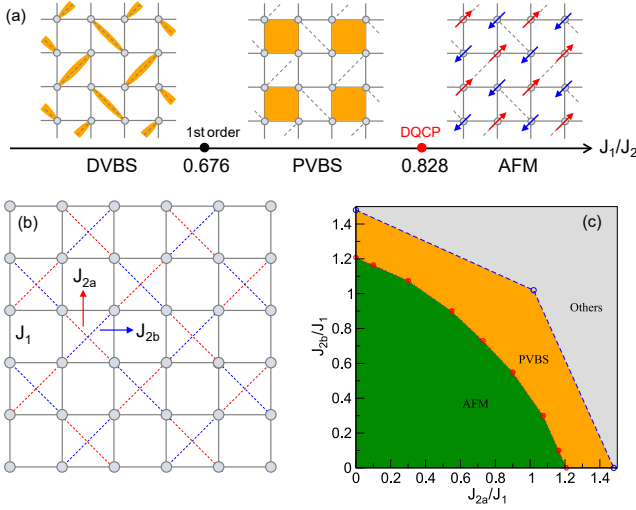


Figure 1. (a) Ground state phase diagram of the SSM, including three phase: DVBS, PVBS and AFM. Dashed diagonal lines indicate the NNN interaction terms. (b) The extended SSM, which contains two sets of NNN interaction J_{2a} (red) and J_{2b} (blue). (c) Ground state phase diagram of the extended Shastry-Sutherland model and it is symmetric about J_{2a} and J_{2b} . $J_{2b} = 0$ (or $J_{2a} = 0$) corresponds to the SSM, and $J_{2a} = J_{2b}$ corresponds to the checkerboard model (CBM). The grey region denotes other phases not of interest here.

These two models can be tuned to each other by changing J_{2a} and J_{2b} . For the CBM, previous studies suggest a PVBS-AFM transition [44–46]. Our extensive tensor network simulations yield strong evidence that the SSM undergoes a direct PVBS-AFM transition accompanied with emergent $O(4)$ symmetry, supporting a DQCP in the SSM. These results are further supported by the investigations of the extended SSM, which exhibit the same type of DQCP physics. The whole phase diagram is presented in Fig. 1(c). Our findings suggest a very natural way to understand the experimentally observed proximate DQCP phenomena in $\text{SrCu}_2(\text{BO}_3)_2$.

Results of the SSM. The finite PEPS algorithm here we adopt has been demonstrated as a powerful approach for simulating quantum spin systems [23–25, 47–49]. To further verify the finite PEPS results, we carefully compare with DMRG and infinite-size tensor network methods on the SSM [31, 35]. These results explicitly demonstrate the high accuracy of the finite PEPS method. (See Supplemental Material for more details. In addition, we also benchmark our results of $J-Q$ model with Quantum Monte Carlo simulation at all different sizes.) We use $D = 8$ to perform all calculations, where both the ground state energy and order parameters are well converged for the largest available size 20×20 by very careful analysis for $D = 4-10$ results (See Supplemental Material for more details).

Since our method works well for open boundary systems, we first look into the boundary induced dimerized pattern on $L \times L$ systems for the SSM. We set $J_2 = 1$ to keep the same energy scale with previous studies. The local plaquette operator at site $\mathbf{i} = (i_x, i_y)$ is defined as $\Pi_{\mathbf{i}} = \frac{1}{2}(P_{\square, \mathbf{i}} + P_{\square, \mathbf{i}}^{-1})$, where $P_{\square, \mathbf{i}}$ denotes the cyclic exchange operator of

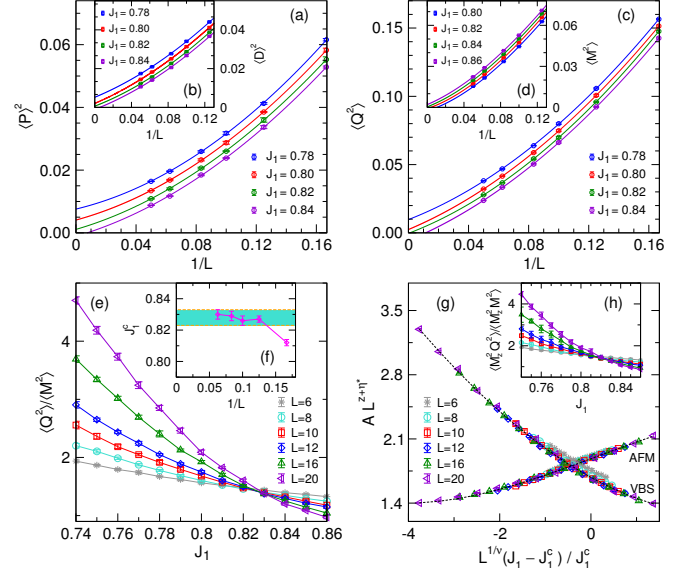


Figure 2. Finite size scaling of ground state order parameters for the SSM on $L \times L$ lattices (a)-(d). Quadratic fits are shown for VBS order parameters (a-c) and cubic fits are shown for AFM order parameter (d) using $L = 6-20$. The ratios of PVBS and AFM order parameters $\langle Q^2 \rangle / \langle M^2 \rangle$ are presented in (e) and their crossing points from $(L, L+2)$ or $(L, L+4)$ are presented in (f). (h) shows the fourth-order momentum ratio. (g) shows the data collapse of PVBS and AFM order parameters, and the dashed lines are quadratic curves using the corresponding critical exponents. The values of scaled AMF quantities in (g) have been shifted upwards by 0.7 for clear display.

the four spins on a given plaquette at site \mathbf{i} . The boundary induced plaquette order parameter is measured by $P = \frac{1}{N_p} \sum_{\mathbf{i}} (-1)^{i_x} \Pi_{\mathbf{i}}$, where $N_p = (L-1)^2$ is the total number of counted plaquettes [50]. The scaling of $\langle P \rangle^2$ with $L = 6-20$ is shown in Fig. 2(a) for different couplings J_1 using second order polynomial fits. With J_1 increasing, $\langle P \rangle^2$ gradually decreases. The extrapolated $\langle P \rangle^2$ in the thermodynamic limit at $J_1 = 0.78, 0.80, 0.82$ are 0.0075(3), 0.0041(3) and 0.0014(5), respectively, but would be zero at $J_1 = 0.84$. This suggests the PVBS phase vanishes around $J_1 = 0.83$. The third order fits give the same conclusion. The plaquette pattern in the PVBS phase is shown in the middle part of Fig. 1(a).

On the other hand, we consider the dimer order parameters for double check, defined as

$$D_\alpha = \frac{1}{N_b} \sum_{\mathbf{i}} (-1)^{i_\alpha} \mathbf{S}_{\mathbf{i}} \cdot \mathbf{S}_{\mathbf{i}+\mathbf{e}_\alpha}, \quad (3)$$

where $\alpha = x$ or y , and $N_b = L(L-1)$ is the corresponding total number of counted bonds along the α direction. For the PVBS phase, the boundary induced dimerization $\langle D \rangle^2 = \langle D_x \rangle^2 + \langle D_y \rangle^2$ should also be finite in the thermodynamic limit. The scaling of $\langle D \rangle^2$ for $J_1 = 0.78, 0.80, 0.82, 0.84$ using $L = 6-20$ is shown in Fig. 2(b), and indeed is consistent with a PVBS phase for $J_1 \lesssim 0.83$.

Now we turn to the PVBS and AFM order parameters defined based on correlation functions. The PVBS order

parameter is defined as $\langle Q^2 \rangle = \langle (D_x - D_y)^2 \rangle$ where $Q = D_x - D_y$ [33]. In Fig. 2(c), the quantity $\langle Q^2 \rangle$ is presented. The finite-size scaling shows $J_1 = 0.8$ has a nonzero PVBS order 0.0024(6) in the thermodynamic limit, and the vanishing point J_1 of PVBS order parameter is very close to that obtained from the scaling of boundary induced quantities $\langle P \rangle^2$ and $\langle D \rangle^2$. On the other hand, the AFM order parameter $\langle \mathbf{M}^2 \rangle$ where $\mathbf{M} = \frac{1}{L^2} \sum_i (-1)^{i_x+i_y} \mathbf{S}_i$ is shown in Fig. 2(d). One can see with J_1 increasing, the AFM order increases, and potentially establishes for $J_1 \geq 0.84$. These results from different physical quantities suggest a direct PVBS-AFM phase transition. By using the crossing points of order parameter ratio, which we will mention later, it gives a PVBS-AFM transition point at $J_1 \simeq 0.83$, consistent with the finite size scaling analysis. The physical quantities vary smoothly about J_1 in our results, indicating a continuous PVBS-AFM transition, though the possibility of weakly first order transition in the thermodynamic limit can not be fully excluded.

The PVBS-AFM transition point in the SSM has been argued as a DQCP with emergent O(4) symmetry through the rotation of three components of AFM order parameter $\mathbf{M} = (M_x, M_y, M_z)$ and one-component PVBS order parameter Q into each other to form a superspin $\mathbf{n} = (M_x, M_y, M_z, Q)$, where $Q = D_x - D_y$ [33]. To check the O(4) symmetry, as we note the SO(3) symmetry for AFM components is well satisfied by observing $\langle M_z^2 \rangle = \frac{1}{3} \langle \mathbf{M}^2 \rangle$ (see SM), we only need to check the additional symmetry formed by M_z and Q . A simple but nontrivial quantity to verify the emergent O(4) symmetry is that the ratio $\langle Q^2 \rangle / \langle \mathbf{M}^2 \rangle$ (or $\langle Q^2 \rangle / \langle M_z^2 \rangle$ as $\langle M_z^2 \rangle = \frac{1}{3} \langle \mathbf{M}^2 \rangle$) should be size-independent at the transition point [7, 17, 51]. In Fig. 2(e), the quantities $\langle Q^2 \rangle / \langle \mathbf{M}^2 \rangle$ for different system size have a crossing point at $J_1 \simeq 0.83$, which is intrinsically close to the PVBS-AFM transition point evaluated by finite size scaling of order parameters. The crossing points show much smaller finite size effects [Fig. 2(f)], which has also been observed in other DQCP studies by Quantum Monte Carlo simulations [7, 17, 51]. These results on one hand provide direct evidence to support the PVBS-AFM transition point as a DQCP with emergent O(4) symmetry, on the other hand give a more accurate evaluation of the transition point $J_1^c = 0.828(5)$, significantly reducing the uncertainties from the finite size extrapolations of order parameters. We also consider higher order momentum ratios of order parameters to check the emergent symmetry [15, 17, 51], which is very challenging to compute. Within our capability, we can only get the fourth-order momentum ratio $\langle M_z^2 Q^2 \rangle / \langle M_z^2 \mathbf{M}^2 \rangle$. Remarkably, $\langle M_z^2 Q^2 \rangle / \langle M_z^2 \mathbf{M}^2 \rangle$ also has a crossing point around $J_1 \simeq 0.83$, shown in Fig. 2(h), further supporting the emergent symmetry.

The extensive data with different system size enable us to precisely extract the corresponding critical exponents. We use the standard finite size scaling formula without subleading corrections [52]:

$$A(J_1, L) = L^{-(z+\eta^*)} F[L^{1/\nu}(J_1 - J_1^c)/J_1^c], \quad (4)$$

where J_1 denotes the coupling constant, and $A(J_1, L)$ denote the AFM order parameters $\langle \mathbf{M}^2 \rangle$ or VBS order parameters

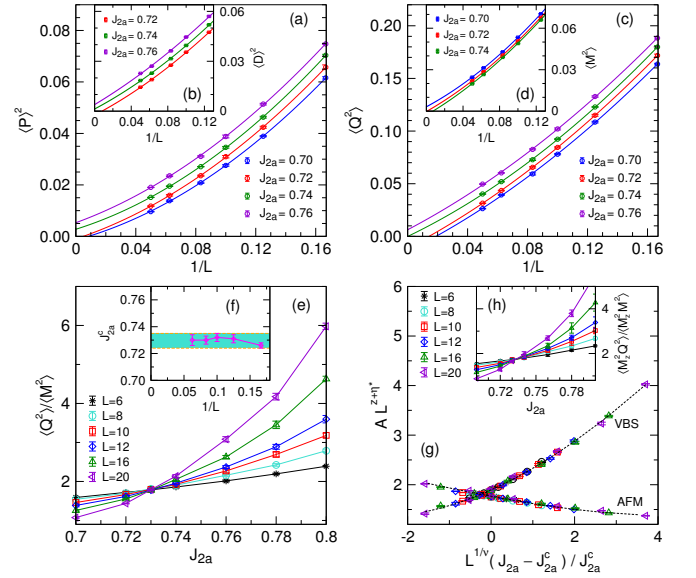


Figure 3. Finite size scaling of ground state order parameters for checkerboard model ($J_{2a} = J_{2b}$) on $L \times L$ lattices (a)-(d), setting $J_1 = 1$. Quadratic fits for $L = 6 - 20$ are shown. The meanings of the figures are the same with those of Fig. 2. The values of scaled AMF quantities in (g) have been shifted upwards by 0.7 for clear display.

$\langle Q^2 \rangle$ for different size L at different J_1 . $z + \eta_{s,p}^*$ represents the spin or plaquette exponents and ν is the correlation length exponent. $F[x]$ is a polynomial function. The analysis of data collapse can be followed in Ref. [24]. In Fig. 2(g), we show the data collapse of the order parameters (using $J_1^c = 0.828(5)$) by collectively fitting $A(J_1, L)$ with different J_1 and L (exclude $L = 6$), and the physical quantities can be well scaled with $z + \eta_s^* = 1.39(2)$, $z + \eta_p^* = 1.39(1)$ and $\nu = 0.84(3)$. On the other hand, note at the critical point $J_1 = J_1^c$ it has $A(J_1^c, L) \propto L^{-(z+\eta^*)}$, indicating that the exponents ($z + \eta^*$) can be directly evaluated by using the data at J_1^c . Indeed at $J_1 = 0.83$ it gives the almost same value 1.39 for both $z + \eta_s^*$ and $z + \eta_p^*$, in good agreement with the collective fittings. Note that the obtained critical exponents clearly indicate $z + \eta_s^* = z + \eta_p^*$, which is consistent with the emergent O(4) symmetry [15, 25, 51].

Results of the extended SSM. To gain more insight into the ground state phase diagram of SSM, we further consider the extended SSM Eq.(2), which is described by a two dimensional space of parameters ($J_{2a}/J_1, J_{2b}/J_1$). For $J_{2b} = 0$ it recovers the SSM (relabel J_{2a} as J_2), and for $J_{2b} = J_{2a}$ it corresponds to the CBM. The two cases can be continuously connected to each other by tuning the strength of J_{2b} terms. For the CBM, previous studies suggested it could have a direct PVBS-AFM transition [44–46]. Here we focus on the region close to the suggested PVBS-AFM transition. In Fig. 3, we present different quantities including boundary induced orders $\langle P \rangle^2$ and $\langle D \rangle^2$, and AFM and PVBS order parameters $\langle \mathbf{M}^2 \rangle$ and $\langle Q^2 \rangle$, as well as the order parameter ratios, with the systems up to 20×20 sites. Similar to the analyses of the SSM, we find a continuous PVBS-AFM transition at $J_{2a}/J_1 = J_{2b}/J_1 \simeq 0.73$ for the CBM, associated with the emergent O(4) symmetry.

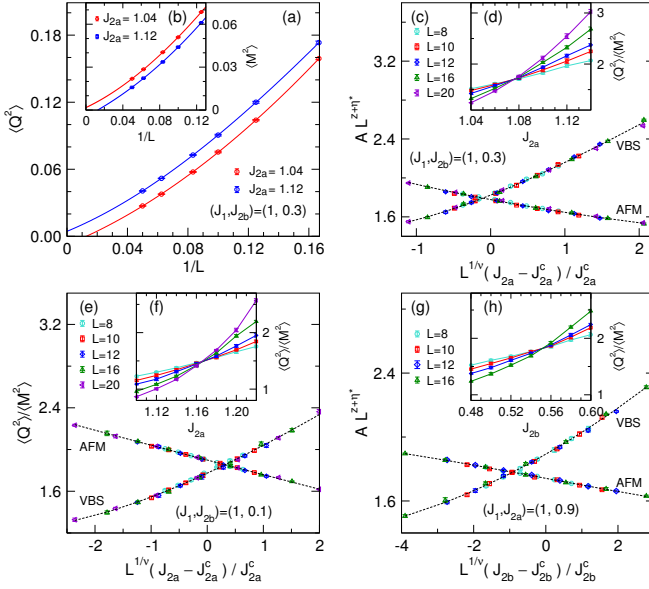


Figure 4. The scaling of AFM and VBS order parameters for three cases: $(J_1, J_{2b}) = (1, 0.3)$ with tuning parameter J_{2a} (a)-(d), and extrapolations with cubic fits for $L = 6 - 20$ are shown (a-b); $(J_1, J_{2b}) = (1, 0.1)$ with tuning parameter J_{2a} (e)-(f); and $(J_1, J_{2a}) = (1, 0.9)$ with tuning parameter J_{2b} (g)-(h). The values of scaled AMF quantities in (c), (e) and (g) have been shifted upwards by 0.7 for clear display.

In fact, by computing the intermediate cases with proper J_{2a}/J_1 and J_{2b}/J_1 in between the SSM and the CBM, we find these different cases also support a continuous PVBS-AFM transition with emergent $O(4)$ symmetry. In Fig. 4, we present the scaling for the cases with fixed $J_{2a}/J_1 = 0.9$ (sweeping J_{2b}), fixed $J_{2b}/J_1 = 0.1$ (sweeping J_{2a}), as well as fixed $J_{2b}/J_1 = 0.3$ (sweeping J_{2a}). In all of these cases, the PVBS has the same plaquette pattern with the SSM that the plaquette singlets are located on four sites without diagonal interaction terms [see Fig.1(b)]. The extracted critical exponents for these different cases are given in Table. I, and it clearly shows that the PVBS-AFM transitions have the similar critical exponents, $z + \eta_s^* = z + \eta_p^* \sim 1.35$ and $\nu \sim 0.80$, suggesting all of them belong to the same universality class. The same value of $z + \eta_s^*$ and $z + \eta_p^*$ is a reflection of the emergent $O(4)$ symmetry. Since the SSM can be smoothly connected to the CBM via the above intermediate cases and the CBM has been consistently suggested to host a PVBS-AFM transition based on our and previous studies, all these results consolidate the existence of a DQCP in the SSM.

Previous DMRG study using level crossing analysis suggests that there is a QSL phase in the region $[g_{c1}, g_{c2}]$ to separate the PVBS and AFM phases for the SSM, where $g_{c1} \approx 0.79$ and $g_{c2} \approx 0.82$ are estimated from DMRG level crossings on finite-size cylindrical systems [37]. However, potential limitations arise because of a small range of sizes L and a further assumption of a $1/L^2$ -dependence for extrapolations [37]. Surprisingly, the extrapolated $g_{c2} = 0.82 \sim 0.83$ [37, 38], is remarkably close to our PVBS-AFM point of $J_1^c = 0.828(5)$. It is possible that g_{c1} would also eventually converge to

Table I. Critical exponents of the extended SSM at the PVBS-AFM transition points. Critical points are from crossing points of the ratio of order parameters. Errors in critical exponents are from fittings.

model	$z + \eta_s^*$	$z + \eta_p^*$	ν	J_c
SSM [$J_{2a} = 1, J_{2b} = 0$]	1.39(2)	1.39(1)	0.84(3)	$J_1 = 0.828(5)$
CBM [$J_1 = 1, J_{2a} = J_{2b}$]	1.33(1)	1.33(1)	0.82(4)	$J_{2a} = 0.730(4)$
$(J_1, J_{2b}) = (1, 0.1)$	1.39(1)	1.39(1)	0.80(4)	$J_{2a} = 1.165(3)$
$(J_1, J_{2b}) = (1, 0.3)$	1.35(1)	1.35(1)	0.85(3)	$J_{2a} = 1.075(4)$
$(J_1, J_{2a}) = (1, 0.9)$	1.33(1)	1.33(1)	0.81(5)	$J_{2b} = 0.550(3)$

the same value with larger sizes and thus the claimed very narrow QSL region is a consequence of finite size effect. Actually, the limitation imposed by the system size can lead to different conclusions. For instance, the iDMRG study on an infinite-size long cylinder that employs the correlation length of excited states, aligns with the finite DMRG level crossing study, but implies a PVBS-AFM transition with emergent $O(4)$ symmetry rather than an intermediate QSL phase [33]. Our extensive results, utilizing larger system sizes, reveal the emergence of $O(4)$ symmetry at the point $J_1^c = 0.828(5)$ in the SSM and similar features in the extended SSM, providing strong evidence for a direct PVBS-AFM transition and significantly diminishing the possibility of an intermediate QSL phase.

Summary and discussion. The physical nature of the PVBS-AFM transition in the SSM is a critical issue to be addressed. By applying the state-of-the-art finite-size tensor network simulations, we reveal a direct continuous PVBS-AFM transition in the SSM, accompanied by emergent $O(4)$ symmetry. Further investigations on the extended SSM, such as the CBM and intermediate variants, show very similar behaviors. These results are consistent with the DQCP nature of PVBS-AFM transition point in the SSM, and exclude the existence of an intermediate QSL phase.

In the SSM, our continuous PVBS-AFM transition at $J_1^c = 0.828(5)$ differs from the weakly first-order transition at $J_1^c \approx 0.78$ that is obtained by the infinite-size tensor network simulations using a finite bond dimension D [31, 35]. These differences in principle could be significantly reduced by properly extrapolating the infinite-size results with new finite correlation length scaling scenarios or using a sufficiently large D [24, 53–56]. While the PVBS-AFM transition in our large-scale simulation is extremely close to a continuous transition, the possibility of a weakly first-order transition in the thermodynamic limit still cannot be fully excluded. Notably, in recent finite-temperature studies [39, 41], in contrast to the first-order DVBS-PVBS transition, no clear sign is found to support a first-order PVBS-AFM transition.

In the PVBS phase of $\text{SrCu}_2(\text{BO}_3)_2$, the plaquette singlets form at the sites with diagonal interactions, which is different from the SSM and is possibly owing to the weak intralayer and interlayer interactions [26–28, 32, 35, 41, 57]. Interestingly, in the phase diagram of $\text{SrCu}_2(\text{BO}_3)_2$, including these extra interactions, the PVBS-AFM transition line in $\text{SrCu}_2(\text{BO}_3)_2$ still may connect the nearby DQCP in the SSM via a triple critical point [35], exhibiting large correlation lengths with emergent symmetry [33]. On the other hand, the PVBS in

$\text{SrCu}_2(\text{BO}_3)_2$ also has two-fold degeneracy, which in presence of magnetic fields also naturally supports the observed $\text{O}(3)$ symmetry. Thus, our findings strongly suggest that it is a highly compelling scenario that the proximate DQCP phenomena observed in $\text{SrCu}_2(\text{BO}_3)_2$ under magnetic fields, including the emergent $\text{O}(3)$ symmetry and quantum critical scaling at the PVBS-AFM transition [28], can originate from the DQCP in the SSM [33]. Consequently, the anomalous dimension scaling $\eta \sim 0.2$ under magnetic fields in $\text{SrCu}_2(\text{BO}_3)_2$ [28] is understandably near to our result $\eta \sim 0.35$ without magnetic fields (setting the dynamic exponent $z = 1$). Note that the SSM subjected to magnetic fields and additional interactions in $\text{SrCu}_2(\text{BO}_3)_2$, e.g., frustrated bilayer interaction $\sim 0.1J_2$, Dzyaloshinskii–Moriya interaction $\sim 0.03J_2$, and higher-order further-neighbour interaction [41, 57], can possess very rich physics [28, 39–41, 58, 59], and we will leave these studies in the future.

Acknowledgments. We thank Philippe Corboz, Wenan Guo, Wei Li, Frédéric Mila, Junsen Wang, Ning Xi, Zhi-Yuan Xie and Rong Yu for very helpful discussions. We also thank Philippe Corboz and Ning Xi for providing the iPEPS and iPESS data, respectively. This work was supported by the CRF C7012-21GF from the Hong Kong’s Research Grants Council, and the National Key R&D Program of China (Grants No. 2022YFA1403700). W.Q.C. was supported by the National Natural Science Foundation of China (Grants No. 12141402), the Science, Technology and Innovation Commission of Shenzhen Municipality (No. ZDSYS20190902092905285), and the Guangdong Basic and Applied Basic Research Foundation under Grant No. 2020B1515120100. This work was also granted access to the HPC resources of Center for Computational Science and Engineering at Southern University of Science and Technology. X.T.Z. and S.S.G. were supported by the National Natural Science Foundation of China Grants No. 11874078 and No. 11834014. Z.W. was supported by the National Natural Science Foundation of China under Grant No. 12175015.

Supplemental Material

Appendix S-1: Tensor Network Method

The tensor network state, particularly the projected entangled pair state (PEPS), serves as a highly potent description for quantum many-body systems [60]. It has been extensively employed to characterize complex entangled many-body states, including those with topological order [61]. The expressive capacity of PEPS is systematically governed by the dimension D of tensors. In this study, we adopt the tensor network formalism using finite PEPS in the framework of variational Monte Carlo [47, 49], which works very well to deal with open boundary systems. This approach has proven very successful in elucidating the nature of particularly challenging frustrated spin systems [23–25]. The PEPS ansatz here we used is always defined on a square lattice with open boundaries. The tensors on the corners, edges and in the middle region, have 2, 3 and 4 virtual indices, respectively, to connect their nearest neighbour sites. Throughout this paper, unless otherwise specified, we use PEPS with $D = 8$ for all calculations which can provide well-converged results (see Sec. S-1.2). Here we show more results to further demonstrate the accuracy of our method.

1. comparison with QMC on $J - Q$ model

Here we present a comprehensive benchmark study on the spin-1/2 $J - Q$ model, also known as the Heisenberg model with additional four-spin exchange interactions [3]. This model can be unbiasedly simulated using quantum Monte Carlo (QMC) without encountering sign problems and served as a representative example for studying the DQCP [3]. The $J - Q$ model has a VBS-AFM phase transition at $J/Q = 0.0447(2)$ [62]. Due to the existence of four-spin interactions and critical properties for the $J - Q$ model, it thus also offers a highly nontrivial example to demonstrate the capability of PEPS to deal with critical systems.

Here we focus on two commonly studied near critical points: $J/Q = 0$ and $J/Q = 0.1$, which have very large correlation lengths around $\xi \sim 30$ [62]. The QMC results are obtained in the stochastic series expansion (SSE) method [52] on open boundary conditions, which operates in the S_z basis. In this context it is convenient to calculate the z -component quantities, including staggered magnetization $\langle M_z^2 \rangle = \frac{1}{N^2} \langle (\sum_i (-1)^{i_x+i_y} S_i^z)^2 \rangle$ where $N = L^2$, as well as the boundary-induced dimerization $\langle \bar{D} \rangle^2 = \frac{1}{2} (\langle \bar{D}_x \rangle^2 + \langle \bar{D}_y \rangle^2)$, where $\bar{D}_\alpha = \frac{1}{N_b} \sum_i (-1)^{i_\alpha} S_i^z S_{i+e_\alpha}^z$ with $N_b = L(L-1)$.

For the PEPS simulation, we use $D = 8$ PEPS as the variational ansatz, and stochastic gradient descent [47, 49] and stochastic reconfiguration [63] to optimize the PEPS wave function. After optimization, we can compute the physical quantities directly via Monte Carlo sampling of the optimized PEPS. Such energy can also be compared with the one computed from the wave function by symmetrizing the optimized PEPS with horizontal and vertical lattice reflection

and spin inversion symmetry [49], which are listed in Table II. For $L = 20$, the energies using symmetrization at $J/Q = 0$ and 0.1 are -0.77812 and -0.83694 , respectively, slightly lower than -0.77806 and -0.83688 without symmetrization, with a difference around 0.00006 . For $L \leq 16$, with and without symmetrization, the energy differences are also as small as 0.00002 . In all these cases, we find magnetization and dimerization have no visible changes with and without symmetrization, which is similar to the study of the Heisenberg model [49]. The comparison about symmetrization indicates our obtained PEPS is well optimized as a good ground state that can well respect the lattice and spin symmetry.

In Table II, we summarize the physical quantities obtained from QMC and PEPS. It is clear that the obtained physical quantities including energies, magnetization, and dimerization from PEPS are in excellent agreement with those from QMC across different system sizes, and the energy differences can be as small as 0.00009 on 20×20 sites. These results show that $D = 8$ PEPS can produce well converged results up to 20×20 sites, and demonstrate the extraordinary capability of PEPS in handling near critical systems.

2. comparison with DMRG and convergence

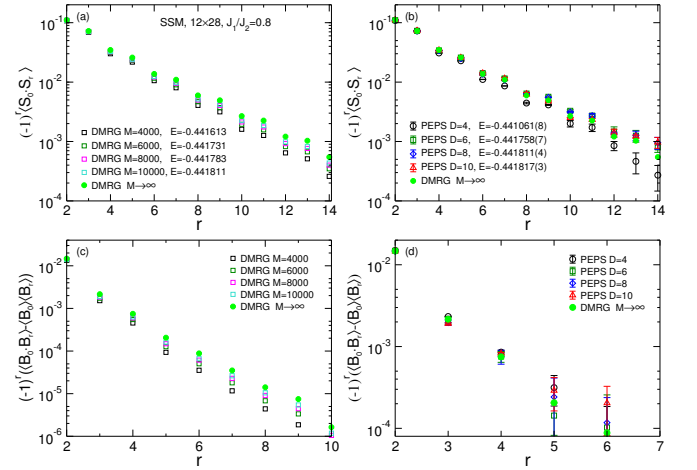


Figure S1. Ground-state energy, spin, and dimer correlation functions from the DMRG and PEPS simulations on the 12×28 SSM at $J_1/J_2 = 0.8$. M is the number of $SU(2)$ multiplets in the DMRG simulations with $SU(2)$ symmetry. The correlation functions are measured along the central row $y = 6$. The reference site for spin correlation is chosen at the third column near the left edge. The dimer correlations are measured for the nearest-neighbor bonds along the x direction with the reference bond located between the third and fourth columns.

Now we directly compare the PEPS and DMRG results of the SSM on a long $L_y \times L_x$ strip with $L_y = 12$, $L_x = 28$. Here we focus on $J_1/J_2 = 0.8$ (set $J_2 = 1$), which is close to the critical point and the nature of which is controversial according to previous studies. The strip geometry has open boundary conditions along both the x - and y -directions. The

Table II. Comparison between PEPS and QMC results on $J-Q$ model on open boundary systems, including ground state energies (set $Q = 1$), magnetizations $\langle M_z^2 \rangle$ and dimerizations $\langle \tilde{D} \rangle^2$. In PEPS calculations, Monte Carlo sampling errors are order of 10^{-6} for energies E_{PEPS} and order of 10^{-5} for $\langle M_z^2 \rangle$ and $\langle \tilde{D} \rangle^2$. For QMC results $\beta = 120$ is used, and sampling errors for these quantities are order of 10^{-6} .

$J/Q = 0$							$J/Q = 0.1$					
L	E_{PEPS}	E_{QMC}	$\langle M_z^2 \rangle_{PEPS}$	$\langle M_z^2 \rangle_{QMC}$	$\langle \tilde{D} \rangle_{PEPS}^2$	$\langle \tilde{D} \rangle_{QMC}^2$	E_{PEPS}	E_{QMC}	$\langle M_z^2 \rangle_{PEPS}$	$\langle M_z^2 \rangle_{QMC}$	$\langle \tilde{D} \rangle_{PEPS}^2$	$\langle \tilde{D} \rangle_{QMC}^2$
6	-0.66172	-0.66174	0.02531(8)	0.02539	0.00572(2)	0.00565	-0.71708	-0.71711	0.02665(6)	0.02672	0.00533(2)	0.00526
8	-0.70379	-0.70383	0.01565(9)	0.01573	0.00433(2)	0.00430	-0.76015	-0.76019	0.01670(3)	0.01684	0.00396(1)	0.00392
10	-0.72897	-0.72903	0.01074(6)	0.01092	0.00355(1)	0.00349	-0.78603	-0.78608	0.01175(3)	0.01187	0.00316(0)	0.00312
12	-0.74558	-0.74564	0.00804(4)	0.00812	0.00298(3)	0.00295	-0.80318	-0.80322	0.00890(4)	0.00898	0.00262(1)	0.00258
14	-0.75735	-0.75739	0.00633(2)	0.00634	0.00260(1)	0.00256	-0.81534	-0.81539	0.00704(4)	0.00712	0.00224(2)	0.00219
16	-0.76606	-0.76613	0.00507(3)	0.00513	0.00231(2)	0.00227	-0.82440	-0.82446	0.00577(3)	0.00585	0.00194(1)	0.00191
20	-0.77812	-0.77820	0.00353(2)	0.00360	0.00192(1)	0.00186	-0.83694	-0.83703	0.00412(3)	0.00424	0.00157(1)	0.00151

DMRG simulations with spin SU(2) symmetry use a maximum bond dimension of $M = 10000$ SU(2) multiplets, which is equivalent to about 40000 U(1) states and ensures a good convergence with the truncation error at about 1×10^{-6} . The ground-state energy per site for each M is listed in the legend of Fig. S1(a). The DMRG correlation functions are measured along the central row ($y = 6$) and are extrapolated versus $1/M$ ($M = 4000 - 10000$) following a second order polynomial fit. The extrapolated results are shown by the green filled circles in Figs. S1(a) and S1(c). For the spin correlation function $\langle \mathbf{S}_0 \cdot \mathbf{S}_r \rangle$, the reference site \mathbf{S}_0 is chosen at the third column near the left edge. For the dimer correlation function $\langle B_0 B_r \rangle - \langle B_0 \rangle \langle B_r \rangle$, the bond operators are chosen along the x direction, namely $B_r = \mathbf{S}_r \cdot \mathbf{S}_{r+\hat{x}}$ (\hat{x} is the unit vector along the x direction). The reference bond for dimer correlations is chosen between the third and fourth columns near the left boundary.

The PEPS results from $D = 4 - 10$ are also presented to compare with the DMRG results. Firstly, we note that the PEPS energies at $D = 8$ and 10 agree very well with the $M = 10000$ DMRG energy. Meanwhile, the converged PEPS correlations also agree very well with those obtained from DMRG, as shown in Figs. S1(b) and S1(d). These comparisons further demonstrate the accuracy of our PEPS results. It also shows that the PEPS simulations with $D = 8$ are good enough to converge the results for the 12×28 SSM.

Here we explicitly show the convergence of energy and order parameters on the largest available 20×20 SSM system at $J_1/J_2 = 0.8$, shown in Table. III. In the calculations, for the order parameters $\langle M^2 \rangle$ and $\langle Q^2 \rangle$ defined based on correlation functions, all pairs of spin and dimer correlations are computed for summation, respectively. Other order parameters mainly involve local terms, which have less computational cost and can be obtained with smaller sampling uncertainty, allowing to check the convergence in higher accuracy. Similar to 12×28 , for 20×20 we can see visible improvement by increasing $D = 4$ to $D = 8$, and the $D = 6$ results are rather close to $D = 8$ results. Further increasing D to 10, the results almost have no further visible improvement, indicating $D = 8$ indeed converges well for the physical quantities. Actually, it has also been shown that the $D = 8$ PEPS simulations can converge quite well for other highly frustrated spin models [23–25], including the J_1 - J_2 - J_3 model up to 20×28 sites [24], as well as the above highly nontrivial

$J-Q$ model. In the meanwhile, in Table. III, we can see for large D it has $\langle M^2 \rangle = 3\langle M_z^2 \rangle$ and $\langle M_z \rangle$ is almost zero within the Monte Carlo sampling error where $M_z = \frac{1}{L^2} \sum_{i_x, i_y} (-1)^{i_x+i_y} S_{i_x, i_y}^z$, indicating the SU(2) symmetry of the ground state recovers very well.

3. comparison with iPEPS and iPESS

We conduct a comparison of energy per site between the finite PEPS and iPEPS methods, shown in Fig. S2. For this purpose, we utilize the best iPEPS energies reported in Ref. [31] at $J_1/J_2 = 0.75, 0.76, 0.77$, and 0.78 , all obtained with a bond dimension of $D = 10$. To obtain the thermodynamic limit energy for our finite size calculations, we perform an extrapolation of the finite PEPS energy using systems with sizes ranging from $L = 6$ to $L = 20$. To facilitate finite-size scaling, one can choose different central cluster $\tilde{L} \times \tilde{L}$ for finite-size scaling [23, 24, 49], as depicted in Fig. S2. Regardless of the chosen central cluster, the extrapolated energies for each J_1/J_2 remain almost identical, similar to previous studies [23, 24, 49]. These extrapolated PEPS energies and iPEPS energies show a nice agreement with up to 5 significant digits.

We also compare the SSM energies at $J_1/J_2 = 0.8$ with other available results, here from the infinite-size projected entangled simplex states (iPESS) results, shown in Fig. S3. The best iPESS result ($D = 7$) is taken from Ref. [31]. We can see the extrapolated finite PEPS energies also agree well with the iPESS results up to 4 significant digits.

Similar to the iPEPS analysis in Ref. [31], we can determine the first-order transition point between the DVBS (dimer valence-bond solid) and PVBS (plaquette valence-bond solid) phases by examining the ground state energy. The DVBS phase corresponds to a dimer state with an exact energy $E_{DVBS} = -0.375$. Using finite size scaling, we can get the thermodynamic limit energies at $J_1/J_2 = 0.68$ and 0.72 , and estimate the energies at other J_1/J_2 points with a presumed linear extrapolation with respect to J_1/J_2 (a linear assumption is reasonable as the energy seems to change linearly in a large range of J_1/J_2 according to our results or previous studies [31, 33, 35]). The energy variation about J_1/J_2 , obviously suggests a first-order DVBS-PVBS transition at $J_1/J_2 \approx 0.676$, shown in Fig. S4, which is also in good

Table III. The convergence of energy and order parameters with respect to the PEPS bond dimension D on the 20×20 SSM system at $J_1/J_2 = 0.8$ (set $J_2 = 1$). $\langle P \rangle^2$, $\langle D \rangle^2$ and $\langle Q^2 \rangle$ are all valid VBS order parameters, used for cross check; $\langle M^2 \rangle$ are AFM order parameters, and $3\langle M_z^2 \rangle$ and $\langle M_z \rangle$ are used to check the SU(2) symmetry.

D	E	$\langle P \rangle^2$	$\langle D \rangle^2$	$\langle Q^2 \rangle$	$\langle M^2 \rangle$	$3\langle M_z^2 \rangle$	$\langle M_z \rangle$
4	-0.442104(8)	0.01624(8)	0.01738(9)	0.0380(2)	0.0139(1)	0.01450(9)	0.0014(4)
6	-0.442861(9)	0.01349(5)	0.01454(5)	0.0324(1)	0.0158(1)	0.01571(9)	0.0011(5)
8	-0.442920(2)	0.01341(8)	0.01442(9)	0.0321(2)	0.0155(1)	0.01548(6)	0.0001(5)
10	-0.442928(3)	0.01344(9)	0.01441(5)	0.0320(1)	0.0155(2)	0.01549(5)	0.0003(4)

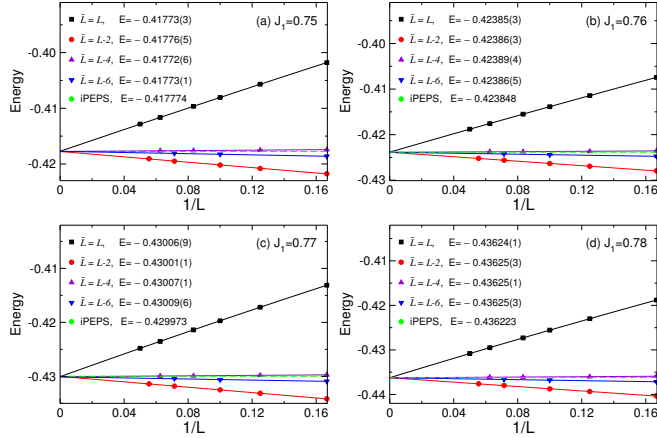


Figure S2. Finite size scaling of ground state energies with $L = 6 - 20$ for SSM at different J_1 . The iPEPS results are from Ref. [31]. For $\tilde{L} = L$ second-order polynomial fits are used and for other cases, linear fits are used. Extrapolated thermodynamic limit energies are listed in the legend.

agreement with the iPEPS and iPESS results, as well as other studies [33].

Appendix S-2: Setup for open boundary systems

In open boundary systems, the presence of boundaries will induce dimerized patterns, which requires careful consideration about such effects on the real plaquette pattern in the PVBS phase. To illustrate this, we examine the Shastry-Sutherland model (SSM) and calculate the values of local plaquette operators at each site.

We start by considering setup A, where diagonal interaction terms exist at the corners. We consider an $L \times L$ lattice with $L = 20$. We observe a distinct plaquette pattern near the boundaries of the systems, but it becomes blurry in the middle region, shown in Fig. S5(a). This blurriness is a consequence of the boundaries. Specifically, the x -directional boundaries induce a certain pattern, while the y -directional boundaries give rise to another kind of plaquette pattern. The 'superposition' of these equal-footing boundary effects results in the formation of domain walls along the diagonal directions [see Fig. S5(a)]. However, if the x - and y -boundaries are not treated on equal footing, a clear plaquette pattern may eventually emerge in the middle region, as illustrated in Fig. S5(b) for a 16×28 system.

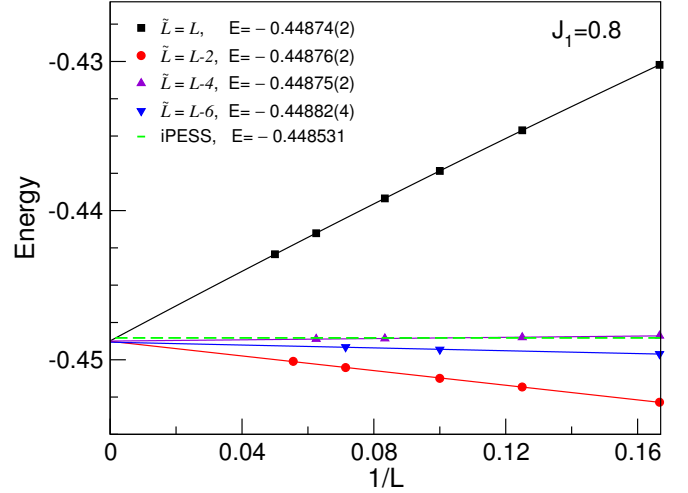


Figure S3. Finite size scaling of ground state energies with $L = 6 - 20$ for SSM at $J_1 = 0.8$. The iPESS results are from Ref. [35]. For $\tilde{L} = L$ second-order polynomial fits are used and for other cases, linear fits are used. Extrapolated thermodynamic limit energies are listed in the legend.

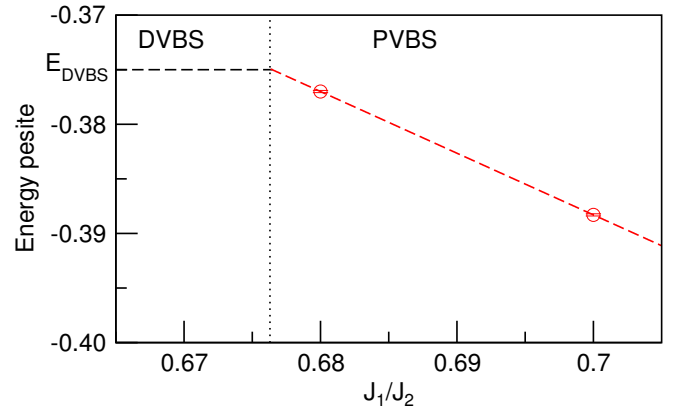


Figure S4. Energy variation with respect to J_1/J_2 for the SSM. Red points denote thermodynamic limit energies at $J_1/J_2 = 0.68$ and 0.72 , and red dashed line denotes a presumed linear change of the energies close to the first-order transition point.

In setup A, the presence of domain walls poses a challenge for finite-size scaling since the VBS order parameters defined on the entire lattice are not well-defined due to the incompatibility of the plaquette pattern in different domains. For example, considering the boundary-induced plaquette

order parameter $P = \frac{1}{N_p} \sum_i (-1)^{i_x} \Pi_i$, the contributions from different domains could be partly canceled (so is the VBS order parameters based on bond-bond correlations). Even if one attempts to define the VBS order parameters within a specific domain, the ambiguity caused by the domain walls cannot be entirely removed.

The plaquette pattern in the middle region of 16×28 system using setup A [Fig. S5(b)], suggests one should use

the setup B, where corner sites have no diagonal interaction terms. In this context, the plaquette pattern is compatible with the boundaries [see Fig. S5(c)]. As a result, there are no domain walls, and the VBS order parameters can be defined unambiguously over the lattice, which ensures a more reliable and consistent analysis of the VBS order parameters. Consequently, throughout this work, setup B is used to compute all physical quantities in the SSM and the extended SSM.

-
- [1] T. Senthil, Ashvin Vishwanath, Leon Balents, Subir Sachdev, and Matthew P. A. Fisher, “Deconfined quantum critical points,” *Science* **303**, 1490–1494 (2004).
 - [2] T. Senthil, Leon Balents, Subir Sachdev, Ashvin Vishwanath, and Matthew P. A. Fisher, “Quantum criticality beyond the Landau-Ginzburg-Wilson paradigm,” *Phys. Rev. B* **70**, 144407 (2004).
 - [3] Anders W. Sandvik, “Evidence for deconfined quantum criticality in a two-dimensional Heisenberg model with four-spin interactions,” *Phys. Rev. Lett.* **98**, 227202 (2007).
 - [4] Roger G. Melko and Ribhu K. Kaul, “Scaling in the fan of an unconventional quantum critical point,” *Phys. Rev. Lett.* **100**, 017203 (2008).
 - [5] F.-J. Jiang, M. Nyfeler, S. Chandrasekharan, and U.-J. Wiese, “From an antiferromagnet to a valence bond solid: evidence for a first-order phase transition,” *Journal of Statistical Mechanics: Theory and Experiment* **2008**, P02009 (2008).
 - [6] Jie Lou, Anders W. Sandvik, and Naoki Kawashima, “Antiferromagnetic to valence-bond-solid transitions in two-dimensional $SU(N)$ Heisenberg models with multispin interactions,” *Phys. Rev. B* **80**, 180414 (2009).
 - [7] Adam Nahum, P. Serna, J. T. Chalker, M. Ortuño, and A. M. Somoza, “Emergent $SO(5)$ symmetry at the Néel to valence-bond-solid transition,” *Phys. Rev. Lett.* **115**, 267203 (2015).
 - [8] D. Charrier and F. Alet, “Phase diagram of an extended classical dimer model,” *Phys. Rev. B* **82**, 014429 (2010).
 - [9] Anders W. Sandvik, “Continuous quantum phase transition between an antiferromagnet and a valence-bond solid in two dimensions: Evidence for logarithmic corrections to scaling,” *Phys. Rev. Lett.* **104**, 177201 (2010).
 - [10] Ribhu K. Kaul, “Quantum criticality in $SU(3)$ and $SU(4)$ antiferromagnets,” *Phys. Rev. B* **84**, 054407 (2011).
 - [11] Matthew S. Block, Roger G. Melko, and Ribhu K. Kaul, “Fate of \mathbb{CP}^{N-1} fixed points with q monopoles,” *Phys. Rev. Lett.* **111**, 137202 (2013).
 - [12] Kenji Harada, Takafumi Suzuki, Tsuyoshi Okubo, Haruhiko Matsuo, Jie Lou, Hiroshi Watanabe, Syngae Todo, and Naoki Kawashima, “Possibility of deconfined criticality in $su(n)$ Heisenberg models at small n ,” *Phys. Rev. B* **88**, 220408 (2013).
 - [13] Kun Chen, Yuan Huang, Youjin Deng, A. B. Kuklov, N. V. Prokof’ev, and B. V. Svistunov, “Deconfined criticality flow in the Heisenberg model with ring-exchange interactions,” *Phys. Rev. Lett.* **110**, 185701 (2013).
 - [14] Sumiran Pujari, Fabien Alet, and Kedar Damle, “Transitions to valence-bond solid order in a honeycomb lattice antiferromagnet,” *Phys. Rev. B* **91**, 104411 (2015).
 - [15] Adam Nahum, J. T. Chalker, P. Serna, M. Ortuño, and A. M. Somoza, “Deconfined quantum criticality, scaling violations, and classical loop models,” *Phys. Rev. X* **5**, 041048 (2015).
 - [16] Hui Shao, Wenan Guo, and Anders W. Sandvik, “Quantum criticality with two length scales,” *Science* **352**, 213–216 (2016).
 - [17] G. J. Sreejith, Stephen Powell, and Adam Nahum, “Emergent $SO(5)$ symmetry at the columnar ordering transition in the classical cubic dimer model,” *Phys. Rev. Lett.* **122**, 080601 (2019).
 - [18] F. F. Assaad and Tarun Grover, “Simple fermionic model of deconfined phases and phase transitions,” *Phys. Rev. X* **6**, 041049 (2016).
 - [19] Toshihiro Sato, Martin Hohenadler, and Fakher F. Assaad, “Dirac fermions with competing orders: Non-Landau transition with emergent symmetry,” *Phys. Rev. Lett.* **119**, 197203 (2017).
 - [20] Yi-Zhuang You, Yin-Chen He, Cenke Xu, and Ashvin Vishwanath, “Symmetric fermion mass generation as deconfined quantum criticality,” *Phys. Rev. X* **8**, 011026 (2018).
 - [21] Xue-Feng Zhang, Yin-Chen He, Sebastian Eggert, Roderich Moessner, and Frank Pollmann, “Continuous easy-plane deconfined phase transition on the Kagome lattice,” *Phys. Rev. Lett.* **120**, 115702 (2018).
 - [22] Y. Liu, Z. Wang, T. Sato, M. Hohenadler, C. Wang, W. Guo, and F. F. Assaad, “Superconductivity from the condensation of topological defects in a quantum spin-Hall insulator,” *Nat Commun* **10**, 2658 (2019).
 - [23] Wen-Yuan Liu, Shou-Shu Gong, Yu-Bin Li, Didier Poilblanc, Wei-Qiang Chen, and Zheng-Cheng Gu, “Gapless quantum spin liquid and global phase diagram of the spin-1/2 $J_1 - J_2$ square antiferromagnetic Heisenberg model,” *Science Bulletin* **67**, 1034–1041 (2022).
 - [24] Wen-Yuan Liu, Juraj Hasik, Shou-Shu Gong, Didier Poilblanc, Wei-Qiang Chen, and Zheng-Cheng Gu, “Emergence of gapless quantum spin liquid from deconfined quantum critical point,” *Phys. Rev. X* **12**, 031039 (2022).
 - [25] Wen-Yuan Liu, Shou-Shu Gong, Wei-Qiang Chen, and Zheng-Cheng Gu, “Emergent symmetry in quantum phase transition: From deconfined quantum critical point to gapless quantum spin liquid,” *arXiv:2212.00707* (2022).
 - [26] M. E. Zayed, Ch. Rüegg, A. M. Läuchli, C. Panagopoulos, S. S. Saxena, M. Ellerby, D. F. McMorrow, Th. Strässle, S. Klotz, G. Hamel, *et al.*, “4-spin plaquette singlet state in the Shastry–Sutherland compound $\text{SrCu}_2(\text{BO}_3)_2$,” *Nat. Phys.* **13**, 962–966 (2017).
 - [27] Jing Guo, Guangyu Sun, Bowen Zhao, Ling Wang, Wenshan Hong, Vladimir A. Sidorov, Nvsn Ma, Qi Wu, Shiliang Li, Zi Yang Meng, Anders W. Sandvik, and Liling Sun, “Quantum phases of $\text{SrCu}_2(\text{BO}_3)_2$ from high-pressure thermodynamics,” *Phys. Rev. Lett.* **124**, 206602 (2020).
 - [28] Yi Cui, Lu Liu, Huihang Lin, Kai-Hsin Wu, Wenshan Hong, Xuefei Liu, Cong Li, Ze Hu, Ning Xi, Shiliang Li, Rong Yu,

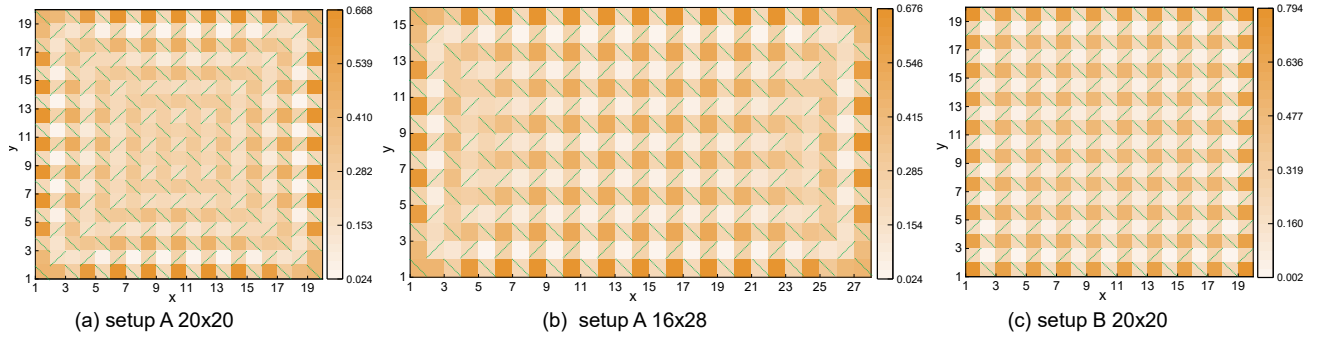


Figure S5. Two setups for the SSM. Green diagonal line denote diagonal interaction terms. Corner sites have diagonal interaction terms in setup A and but not in setup B. (a-b) show the plaquette operator values Π_i setup A on 20×20 and 16×28 systems. (c) shows the plaquette values on 20×20 using setup B. All three cases use $J_1/J_2 = 0.74$.

- Anders W. Sandvik, and Weiqiang Yu, “Proximate deconfined quantum critical point in $\text{SrCu}_2(\text{BO}_3)_2$,” *Science* **380**, 1179–1184 (2023).
- [29] B. Sriram Shastry and Bill Sutherland, “Exact ground state of a quantum mechanical antiferromagnet,” *Physica B+C* **108**, 1069–1070 (1981).
- [30] Shin Miyahara and Kazuo Ueda, “Exact dimer ground state of the two dimensional heisenberg spin system $\text{SrCu}_2(\text{BO}_3)_2$,” *Phys. Rev. Lett.* **82**, 3701–3704 (1999).
- [31] Philippe Corboz and Frédéric Mila, “Tensor network study of the Shastry-Sutherland model in zero magnetic field,” *Phys. Rev. B* **87**, 115144 (2013).
- [32] C. Boos, S. P. G. Crone, I. A. Niesen, P. Corboz, K. P. Schmidt, and F. Mila, “Competition between intermediate plaquette phases in $\text{SrCu}_2(\text{BO}_3)_2$ under pressure,” *Phys. Rev. B* **100**, 140413 (2019).
- [33] Jong Yeon Lee, Yi-Zhuang You, Subir Sachdev, and Ashvin Vishwanath, “Signatures of a deconfined phase transition on the Shastry-Sutherland lattice: Applications to quantum critical $\text{SrCu}_2(\text{BO}_3)_2$,” *Phys. Rev. X* **9**, 041037 (2019).
- [34] Tokuro Shimokawa, “Signatures of finite-temperature mirror symmetry breaking in the $S=\frac{1}{2}$ Shastry-Sutherland model,” *Phys. Rev. B* **103**, 134419 (2021).
- [35] Ning Xi, Hongyu Chen, ZY Xie, and Rong Yu, “First-order transition between the plaquette valence bond solid and antiferromagnetic phases of the Shastry-Sutherland model,” *arXiv:2111.07368* (2021).
- [36] Ahmet Keleş and Erhai Zhao, “Rise and fall of plaquette order in the Shastry-Sutherland magnet revealed by pseudofermion functional renormalization group,” *Phys. Rev. B* **105**, L041115 (2022).
- [37] Jianwei Yang, Anders W. Sandvik, and Ling Wang, “Quantum criticality and spin liquid phase in the Shastry-Sutherland model,” *Phys. Rev. B* **105**, L060409 (2022).
- [38] Ling Wang, Yalei Zhang, and Anders W Sandvik, “Quantum spin liquid phase in the Shastry-Sutherland model detected by an improved level spectroscopic method,” *Chinese Physics Letters* **39**, 077502 (2022).
- [39] Junsen Wang, Han Li, Ning Xi, Yuan Gao, Qing-Bo Yan, Wei Li, and Gang Su, “Plaquette singlet transition, magnetic barocaloric effect, and spin supersolidity in the Shastry-Sutherland model,” *arXiv:2302.06596* (2023).
- [40] Zhenzhong Shi, Sachith Dissanayake, Philippe Corboz, William Steinhardt, David Graf, DM Silevitch, Hanna A Dabkowska, TF Rosenbaum, Frédéric Mila, and Sara Haravifard, “Discovery of quantum phases in the Shastry-Sutherland compound $\text{SrCu}_2(\text{BO}_3)_2$ under extreme conditions of field and pressure,” *Nature Communications* **13**, 2301 (2022).
- [41] J Larrea Jiménez, SPG Crone, Ellen Fogh, Mohamed Ezzat Zayed, Rolf Lortz, Ekaterina Pomjakushina, Kaziemerzh Conder, Andreas M Läuchli, Lukas Weber, Stefan Wessel, *et al.*, “A quantum magnetic analogue to the critical point of water,” *Nature* **592**, 370–375 (2021).
- [42] Akihisa Koga and Norio Kawakami, “Quantum phase transitions in the Shastry-Sutherland model for $\text{SrCu}_2(\text{BO}_3)_2$,” *Phys. Rev. Lett.* **84**, 4461–4464 (2000).
- [43] Yoshihiro Takushima, Akihisa Koga, and Norio Kawakami, “Competing spin-gap phases in a frustrated quantum spin system in two dimensions,” *Journal of the Physical Society of Japan* **70**, 1369–1374 (2001).
- [44] Oleg A. Starykh, Akira Furusaki, and Leon Balents, “Anisotropic pyrochlores and the global phase diagram of the checkerboard antiferromagnet,” *Phys. Rev. B* **72**, 094416 (2005).
- [45] R. F. Bishop, P. H. Y. Li, D. J. J. Farnell, J. Richter, and C. E. Campbell, “Frustrated heisenberg antiferromagnet on the checkerboard lattice: J_1 - J_2 model,” *Phys. Rev. B* **85**, 205122 (2012).
- [46] Haiyuan Zou, Fan Yang, and Wei Ku, “Nearly degenerate ground states of a checkerboard antiferromagnet and their bosonic interpretation,” *arXiv:2011.06520* (2020).
- [47] Wen-Yuan Liu, Shao-Jun Dong, Yong-Jian Han, Guang-Can Guo, and Lixin He, “Gradient optimization of finite projected entangled pair states,” *Phys. Rev. B* **95**, 195154 (2017).
- [48] Wen-Yuan Liu, Shaojun Dong, Chao Wang, Yongjian Han, Hong An, Guang-Can Guo, and Lixin He, “Gapless spin liquid ground state of the spin-1/2 J_1 - J_2 Heisenberg model on square lattices,” *Phys. Rev. B* **98**, 241109 (2018).
- [49] Wen-Yuan Liu, Yi-Zhen Huang, Shou-Shu Gong, and Zheng-Cheng Gu, “Accurate simulation for finite projected entangled pair states in two dimensions,” *Phys. Rev. B* **103**, 235155 (2021).
- [50] Bowen Zhao, Phillip Weinberg, and Anders W Sandvik, “Symmetry-enhanced discontinuous phase transition in a two-dimensional quantum magnet,” *Nature Physics* **15**, 678–682 (2019).
- [51] Pablo Serna and Adam Nahum, “Emergence and spontaneous breaking of approximate $O(4)$ symmetry at a weakly first-order deconfined phase transition,” *Phys. Rev. B* **99**, 195110 (2019).
- [52] Anders W. Sandvik, “Computational studies of quantum spin

- systems,” *AIP Conference Proceedings* **1297**, 135–338 (2010).
- [53] Philippe Corboz, Piotr Czarnik, Geert Kapteijns, and Luca Tagliacozzo, “Finite correlation length scaling with infinite projected entangled-pair states,” *Phys. Rev. X* **8**, 031031 (2018).
- [54] Michael Rader and Andreas M. Läuchli, “Finite correlation length scaling in Lorentz-invariant gapless iPEPS wave functions,” *Phys. Rev. X* **8**, 031030 (2018).
- [55] Bram Vanhecke, Juraj Hasik, Frank Verstraete, and Laurens Vanderstraeten, “Scaling hypothesis for projected entangled-pair states,” *Phys. Rev. Lett.* **129**, 200601 (2022).
- [56] H. J. Liao, Z. Y. Xie, J. Chen, Z. Y. Liu, H. D. Xie, R. Z. Huang, B. Normand, and T. Xiang, “Gapless spin-liquid ground state in the $S = 1/2$ kagome antiferromagnet,” *Phys. Rev. Lett.* **118**, 137202 (2017).
- [57] Hiroyuki Nojiri, Hiroshi Kageyama, Kenzo Onizuka, Yutaka Ueda, and Mitsuhiro Motokawa, “Direct observation of the multiple spin gap excitations in two-dimensional dimer system $\text{SrCu}_2(\text{BO}_3)_2$,” *Journal of the Physical Society of Japan* **68**, 2906–2909 (1999).
- [58] Zhenzhong Shi, William Steinhardt, David Graf, Philippe Corboz, Franziska Weickert, Neil Harrison, Marcelo Jaime, Casey Marjerrison, Hanna A Dabkowska, Frédéric Mila, *et al.*, “Emergent bound states and impurity pairs in chemically doped Shastry-Sutherland system,” *Nature Communications* **10**, 2439 (2019).
- [59] T Nomura, P Corboz, A Miyata, S Zherlitsyn, Y Ishii, Y Kohama, YH Matsuda, A Ikeda, C Zhong, H Kageyama, *et al.*, “Unveiling new quantum phases in the Shastry-Sutherland compound $\text{SrCu}_2(\text{BO}_3)_2$ up to the saturation magnetic field,” *Nature Communications* **14**, 3769 (2023).
- [60] F. Verstraete, V. Murg, and J.I. Cirac, “Matrix product states, projected entangled pair states, and variational renormalization group methods for quantum spin systems,” *Advances in Physics* **57**, 143–224 (2008).
- [61] J. Ignacio Cirac, David Pérez-García, Norbert Schuch, and Frank Verstraete, “Matrix product states and projected entangled pair states: Concepts, symmetries, theorems,” *Rev. Mod. Phys.* **93**, 045003 (2021).
- [62] Anders W. Sandvik, “Finite-size scaling and boundary effects in two-dimensional valence-bond solids,” *Phys. Rev. B* **85**, 134407 (2012).
- [63] Tom Vieijra, Jutho Haegeman, Frank Verstraete, and Laurens Vanderstraeten, “Direct sampling of projected entangled-pair states,” *Phys. Rev. B* **104**, 235141 (2021).